CHAPTER 3

SOLUTION METHOD

The solution method to be used in the present study and the verification of its applicability to the mixed convective impinging jet flow considered here are detailed in this chapter.

3.1 Numerical Scheme and Solution Procedures

The governing differential equations given in Chapters 2 are discretized by the SIMPLE algorithm [34] which is a finite volume (FV) method. These discretized equations are solved by the commercial software STAR-CD [35]. More specifically, the differential equations are integrated over the chosen individual computational cells and over a finite time increment in the present transient problem with the values of the dependent variables approximated in terms of those at the cell-centred nodes. For convenience, the general conservation equations can be expressed as

$$\frac{1}{\sqrt{g}}\frac{\partial}{\partial t}\left(\sqrt{g}\,\rho\phi\right)+div\left(\rho\bar{u}\,\phi-\Gamma_{\phi}grad\phi\right)=s_{\phi} \tag{3.1}$$

where $\bar{u}$ represents u, v or w; φ could express any of the dependent variables, like u, v, w and T ; Γ_{ϕ} and s_{ϕ} are respectively the associated diffusion and source coefficients. Here $\sqrt{g}$ is a metric tensor.

Now Eq. (3.1) can be integrated over a closed surface S valid for an arbitrary control volume $\forall$ to give

$$\frac{d}{dt}\int_{\forall}\rho\phi dV+\int_{S}\left(\rho\bar{u}\phi-\Gamma_{\phi}grad\phi\right)\cdot d\vec{S}=\int_{\forall}s_{\phi}dV \tag{3.2}$$

where $\vec{S}$ is the surface vector. If the $\forall$ and S are respectively taken to be the volume V_p and discrete faces $S_j\,(j=1,N_f)$ of a computational cell as that in Fig. 3.1, Eq. (3.2) becomes

$$\frac{d}{dt}\int_{V_p}\rho\phi dV+\sum_{j}\int_{S_j}\left(\rho\bar{u}\phi-\Gamma_{\phi}grad\phi\right)\cdot d\vec{S}=\int_{V_p}s_{\phi}dV \tag{3.3}$$

For convenient discussion, the first and second terms on the left hand side of Eq. (3.3) are represented by T_1 and T_2, respectively. And T_3 represents the right-hand side of Eq. (3.3). Here T_1 is discretised as

$$T_1\approx\frac{(\rho\phi V)_P^n-(\rho\phi V)_P^o}{\delta t} \tag{3.4}$$

where the subscript "P" in Eq. (3.4) means the node P, and the superscripts "n" and "o" denote the new value and old value, respectively.

The second term T_2 can be separated into convection and diffusion terms by the separate contributions C_j and E_j, respectively. Thus T_2 can be approximated by the average value over each face of the cell as

$$T_2\approx\sum_{j}\left(\rho\bar{u}\phi\cdot\vec{S}\right)_j-\sum_{j}\left(\Gamma_{\phi}grad\phi\cdot\vec{S}\right)_j\equiv\sum_{j}C_j-\sum_{j}E_j \tag{3.5}$$

Upwind differencing is used to approximate the convection term C_j as shown in Fig.

3.2:

$$C_j \equiv \left(\rho\bar{u}\cdot\vec{S}\right)_j \cdot \phi_P \qquad \text{,for} \quad F_j \geq 0 \tag{3.6}$$

$$C_j \equiv \left(\rho\bar{u}\cdot\vec{S}\right)_j \cdot \phi_{N+} \qquad \text{,for} \quad F_j < 0 \tag{3.7}$$

and the diffusion term E_j is represented by the face-centred expressions as

$$E_j \approx \Gamma_{\phi,j}\left\{f_j^l\left(\phi_N - \phi_P\right) + \left[\vec{\nabla}\phi\cdot\vec{S} - f_j^l\vec{\nabla}\phi\cdot\vec{d}_{PN}\right]_j\right\} \tag{3.8}$$

where f_j is a geometry factor, $\vec{d}_{PN}$ is the vector from P to N, $\Gamma_{\phi,j}$ is the diffusion coefficient at the surface.

Finally, T_3 can be expressed as

$$T_3 \approx s_1 - s_2\phi_P \tag{3.9}$$

Substitution of the results in Equs. (3.4)-(3.9) into Eq. (3.3) gives

$$\frac{\left(\rho\phi V\right)^n - \left(\rho\phi V\right)^o}{\delta t} + \sum F_j = 0 \tag{3.10}$$

which can be put in a more compact form as

$$A_p\phi_P^n = \sum_m A_m\phi_m^n + s_1 + B_P\phi_P^o \tag{3.11}$$

where A_m represents the effects of the convection and diffusion and $\sum$ denotes the effects of the overall neighbor nodes shown in Fig. 3.2 for the flux discretisation. Besides, A_P is defined as $\sum_m A_m + s_2 + B_P$ and B_P is equal to $\left(\rho V\right)^o/\delta t$.

When implementing the above solution method, the convergence condition is chosen as

$$C_{\phi}^{k} = \sum \left(\left| B_P^n \phi_P^n \right| - \left| B_P^o \phi_P^o \right| \right) < \text{conservative value} \qquad (3.12)$$

We set the conservative values of velocity field as 0.01, pressure field as 0.001 and temperature field as 0.01 in this study. The simulation procedures are briefly illustrated by a flow chart in Fig. 3.3.

3.2 Verification of Numerical Scheme

The computation domain includes the entire injection pipe and the space between two horizontally parallel disks. We will verify the above solution method by two typical ways: the grid test and comparison with the published experimental results.

3.2.1 Grid Test

The grid distribution is frequently an important issue in numerical computation. It affects the efficiency and accuracy of thermofluid analysis. There are many choices of the grid structure and distribution in STAR-CD including hexahedron, tetrahedron, triangular prism, and pyramid, as shown in Fig. 3.4. Considering the model geometry and physical phenomena, we choose the uniform hexahedron cell in the present simulation. Then we use the subdomains of the cell in the numerical solution of the differential conservation equations. The grid distribution for the impinging jet flow investigated here is shown in Fig. 3.5. The corresponding side view and top view of

the half domain are shown in Fig. 3.6. The grid number for the injection pipe is 5 × 36 × 300 and in the space between the disks we have 220 × 36 × 20 grids. Hence a total of 212,400 cells are used in the computation. For the cases with D_j = 10.0 mm, Q_j = 1-5 slpm, and ΔT = 0-25 ℃ the computed results using this grid distribution are compared with those computed from the 53,100 and 309,600 cells. Selected results to compare the computation from these three different grids are shown in Fig. 3.7. It is noted that the results from the 212,400 and 309,600 cells are in good agreement. The differences in the magnitude of velocity computed from these two grid distributions are less than 12%. Thus the chosen grid distribution with the 212, 400 cells is used in the subsequent computation. Then the time interval test is conducted. Sample results from this test are shown in Figs. 3.8 and 3.9 for the case with D_j = 10.0 mm, H = 10.0 mm, Ra = 1,880 (ΔT = 20.0 ℃), Re_j = 270 (Q_j = 2.0 slpm) for three time intervals Δt = 0.05, 0.1, 0.15. The predicted vortex flow patterns revealed from vector velocity maps and contours of velocity components are also in good agreement. Thus we choose the time step Δt = 0.1 in the subsequent computation. Finally, we test the suitable length of the insulated annular section. Selected results for the chosen case computed by two insulated section lengths of 20.0 and 80.0 mm are shown in Figs. 3.10 and 3.11. The predicted vortex flow patterns from using the two insulated section lengths agree well with each other. Thus we choose the length of insulated annular section of 20.0 mm to save the computation time in the present study.

3.2.2 Verification with Experimental Results

To further verify the proposed solution method, the present results are compared with some experimental data reported in the literature. This is illustrated in Fig. 3.12

by comparing our predicted vortex flow pattern with that from Santen et al. [26, 27] for the case with Re = 40, Ra = 3,800 and Pr =0.7 for H = 20.0 mm, D_j = 20.0 mm and D = 500 mm. Note that our prediction is in qualitative agreement with the results from Santen et al. We also note that for this case the vortex flow is unstable. The results shown in Fig. 3.12 are those observed at some time instant in the statistical state. In fact, the vortex flow pattern changes significantly with time during the statistical state.

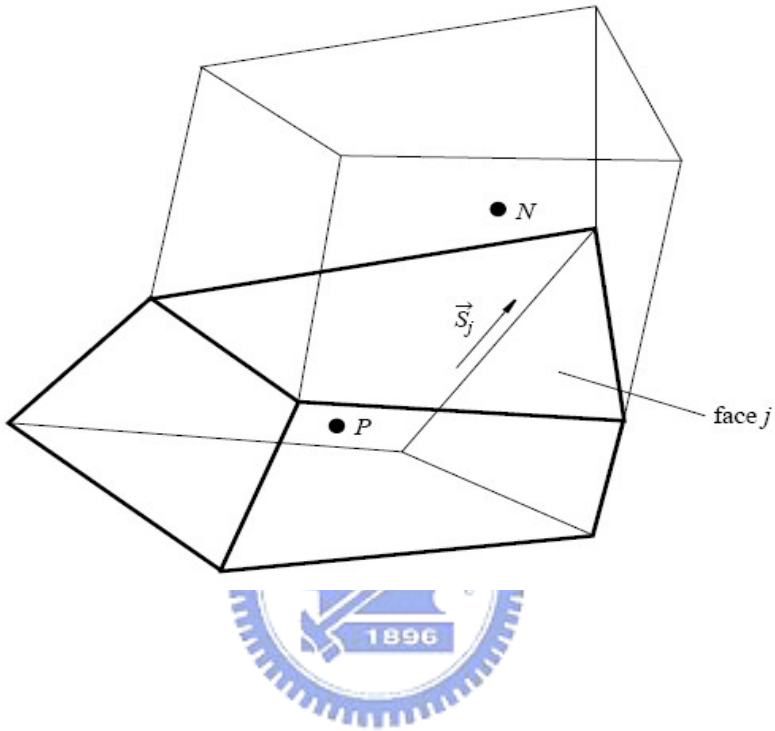

Fig. 3.1 The locations of the centred node P in a typical cell and centred node N in the neighbor cell.

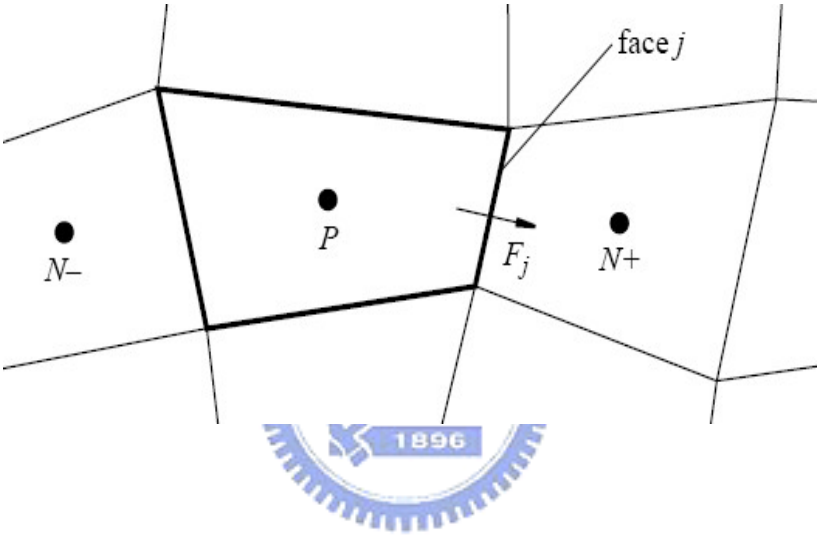

Fig. 3.2 The upwind differencing with node labeling for flux discretization.

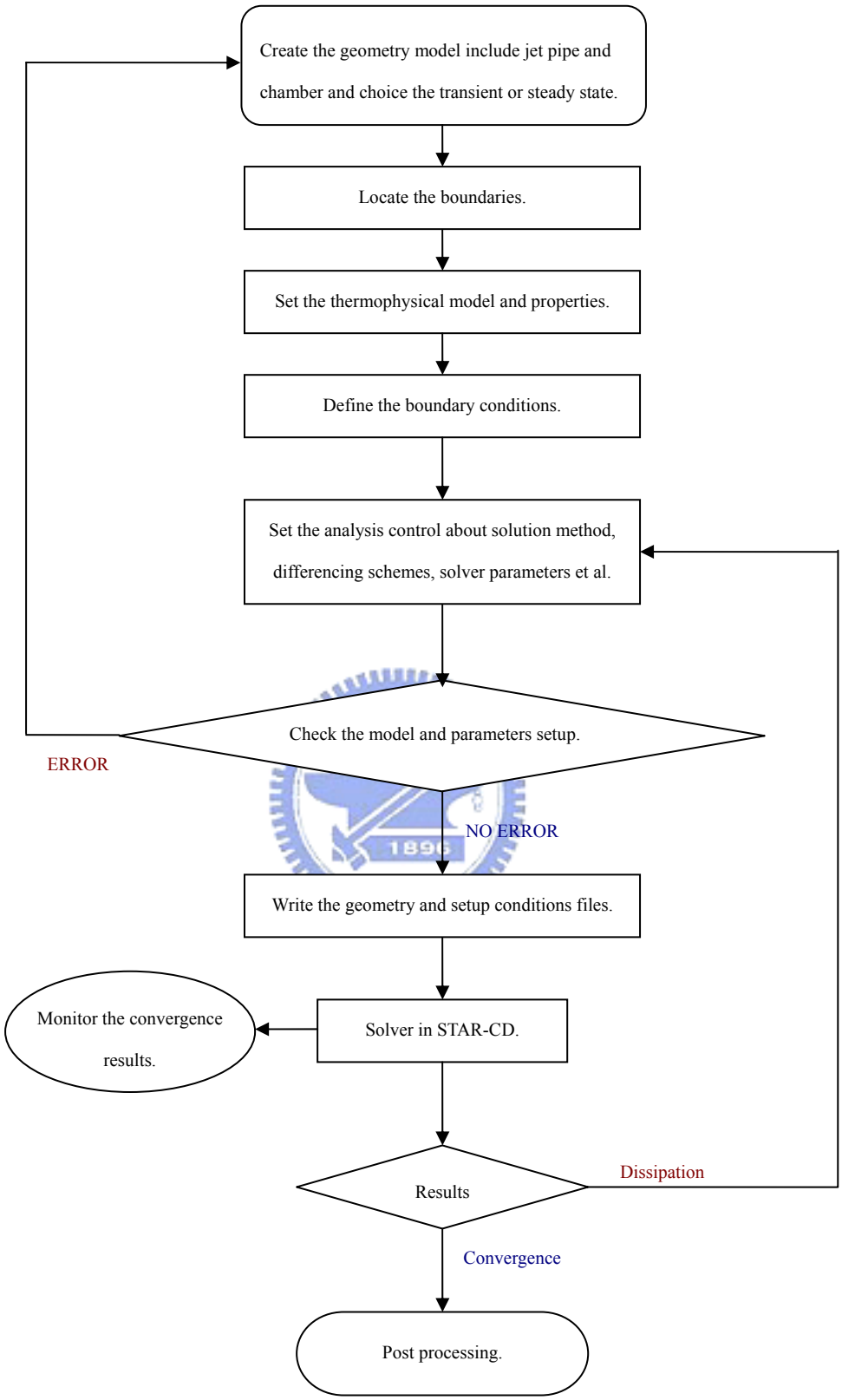

Fig. 3.3 Flow chart for the simulation procedures.

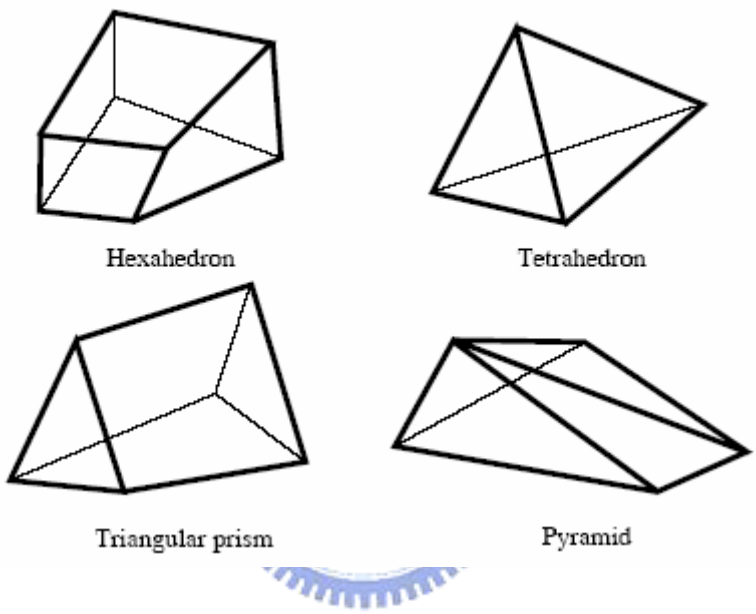

Fig. 3.4 The cell structures available in STAR-CD.

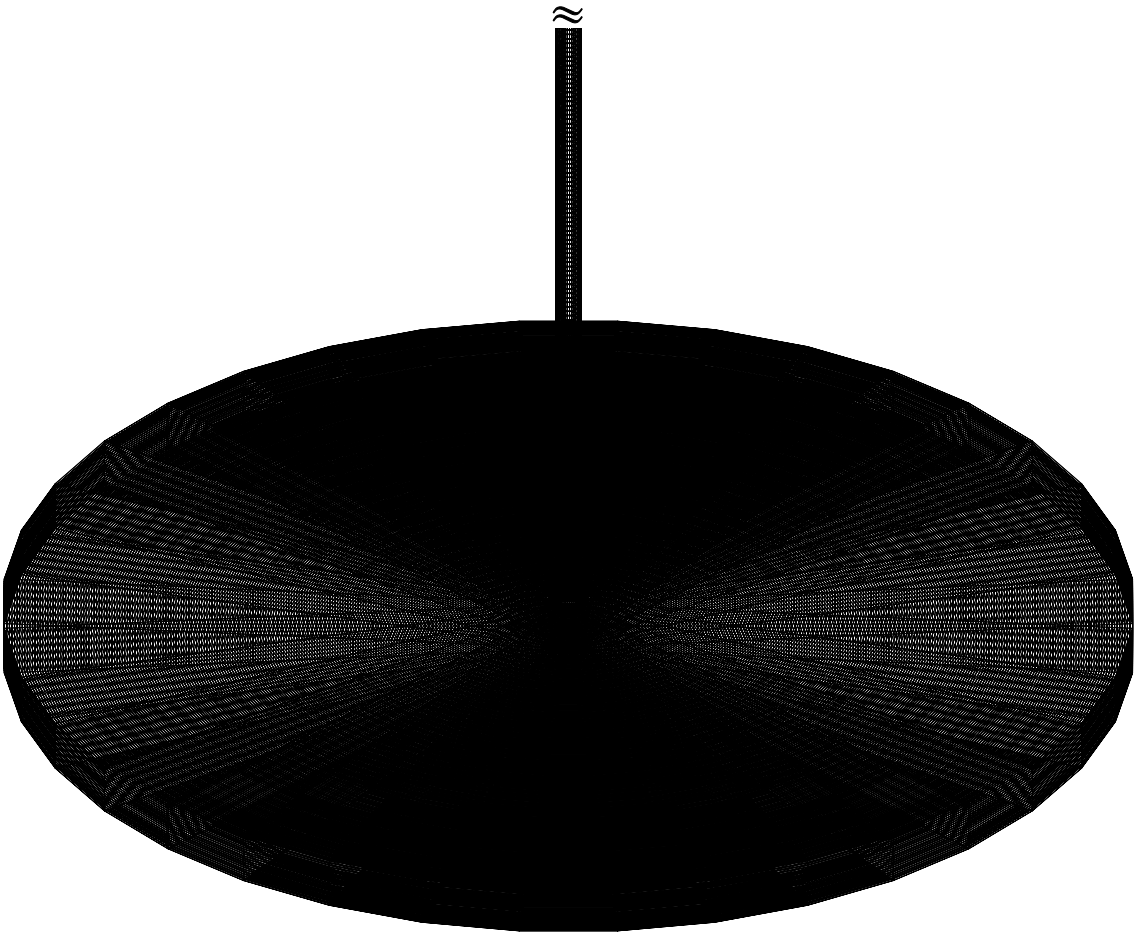

Fig. 3.5 The mesh distribution from the three dimensional view for the chamber and part of the injection pipe.

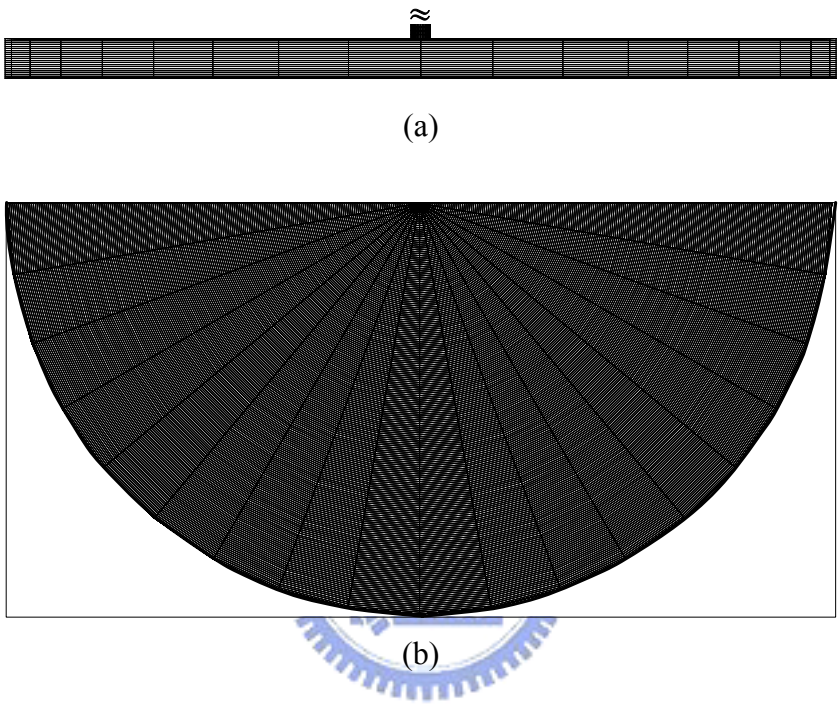

(a)

(b)

Fig. 3.6 The mesh distribution in the chamber from (a) side view at the vertical plane θ=0° & 180° and (b) top view.

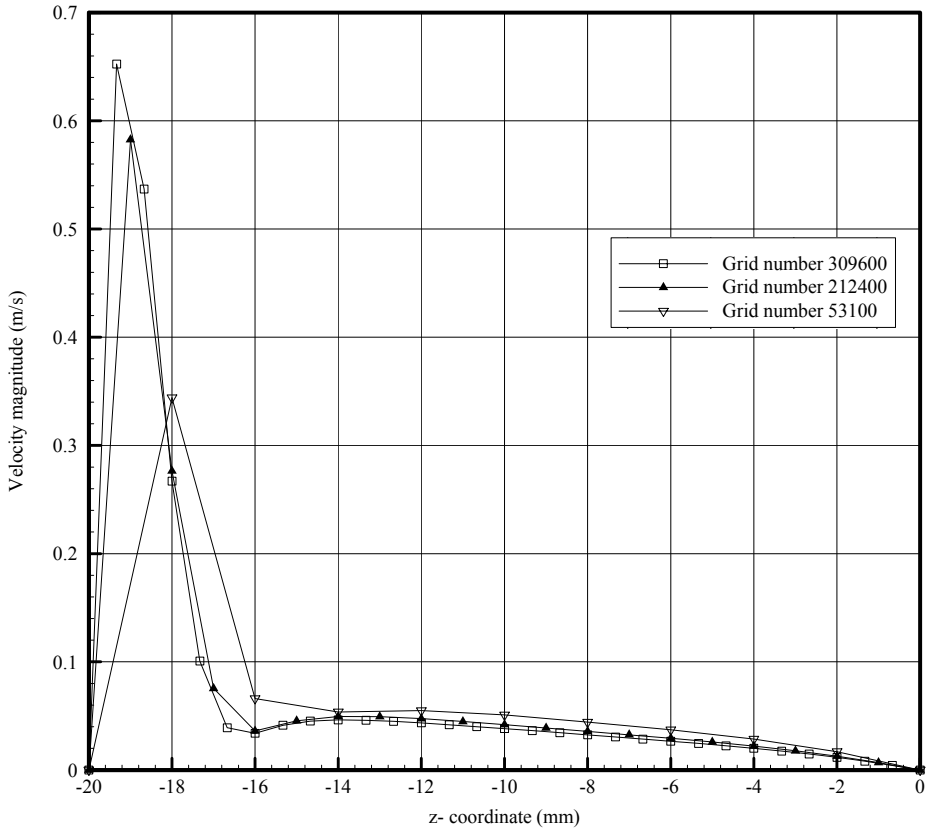

Fig. 3.7 The vertical variations of the steady velocity magnitude at the locations on the line r = 16 mm and $\theta = 0^{\circ}$ predicted from three different grids.

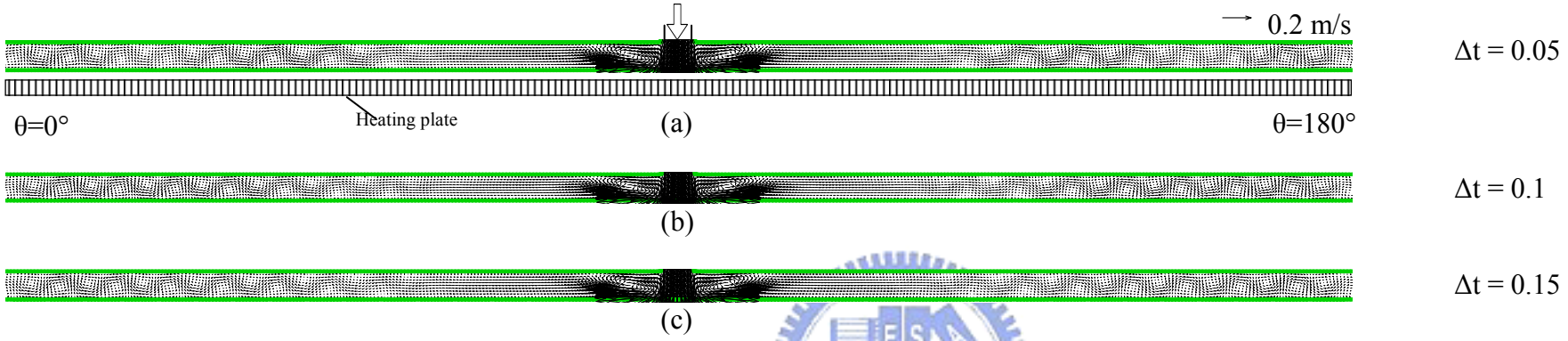

Fig. 3.8 Velocity vectors on the cross plane θ = 0° & 180° at steady state for D_j = 10.0 mm, H = 10.0 mm, Ra = 1,880 (ΔT = 20.0℃), Re_j = 270 (Q_j=2.0slpm) for different time step size Δt = (a) 0.05, (b) 0.1, and (c) 0.15.

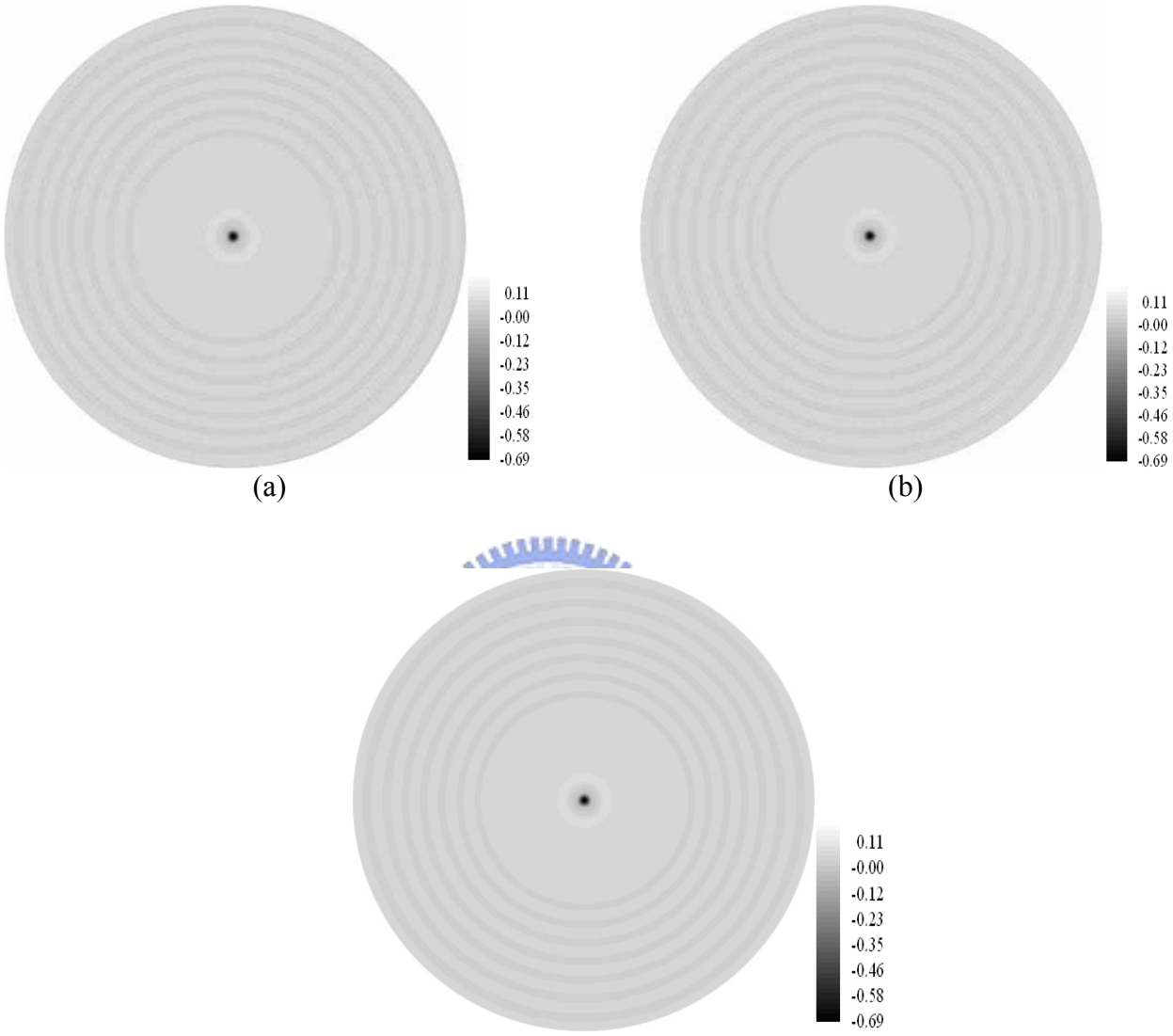

Fig. 3.9 Contours of vertical velocity component w at long time at the horizontal plane at z = - 5.0 mm for D_j = 10.0 mm, H = 10.0 mm, Ra = 1,880 (ΔT = 20.0℃), Re_j = 270 (Q_j=2.0slpm) for different time step size Δt = (a) 0.05, (b) 0.1, and (c) 0.15.

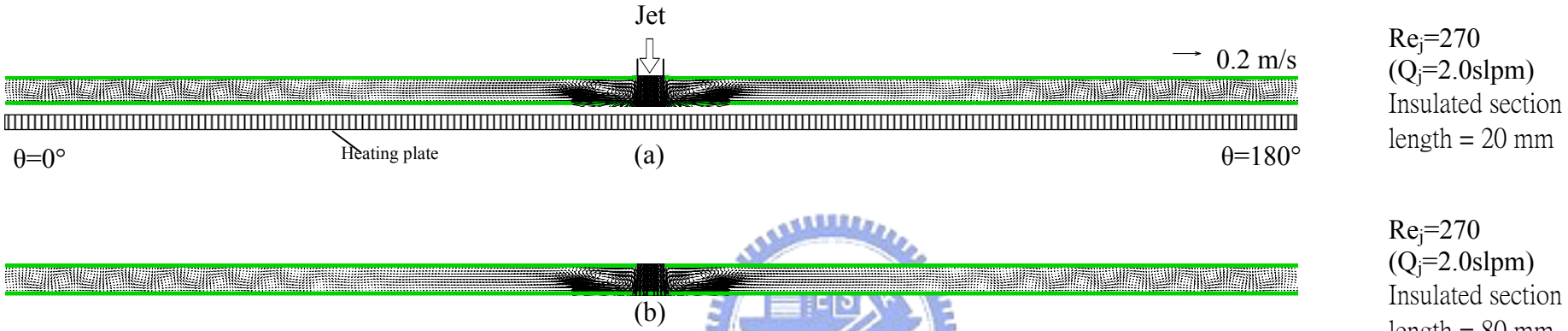

Re_j=270
(Q_j=2.0slpm)
Insulated section
length = 20 mm

Re_j=270
(Q_j=2.0slpm)
Insulated section
length = 80 mm

Fig. 3.10 Velocity vectors on the cross plane θ = 0° & 180° at steady state for D_j = 10.0 mm, H = 10.0 mm, Ra = 1,880 (ΔT = 20.0℃), Re_j = 270 (Q_j=2.0 slpm) for varied lengths of the insulated annular section (a) 20 mm and (b) 80 mm.

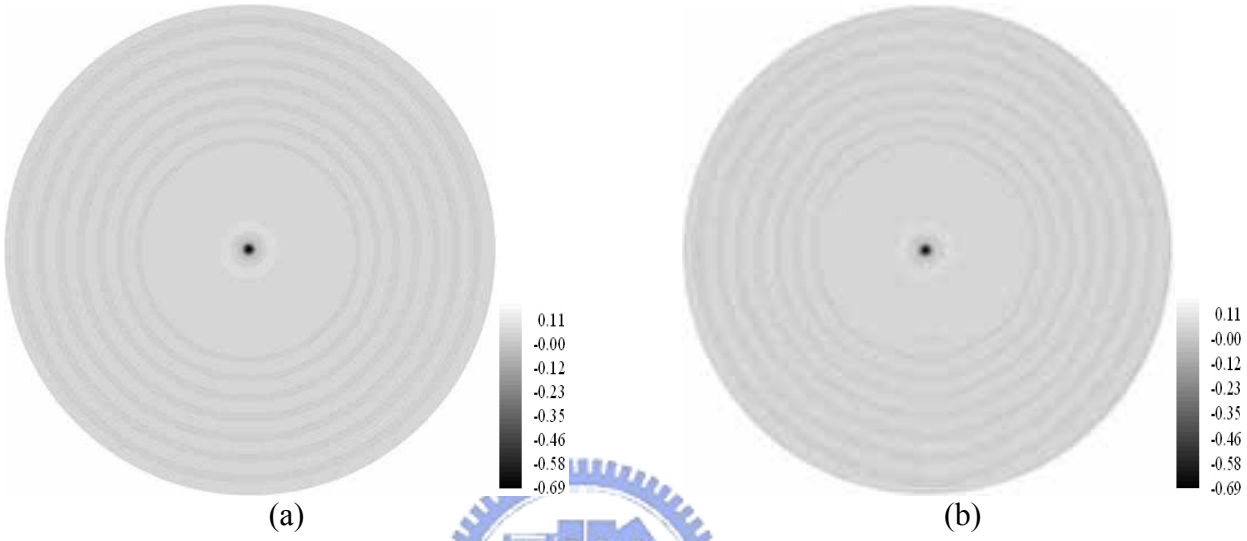

Fig. 3.11 Contours of vertical velocity component w at long time at the horizontal plane at z = - 5 mm for Ra = 1,880 (ΔT = 20.0℃) and D_j = 10.0mm at H = 10.0 mm, Re_j = 270 (Q_j=2.0slpm) for varied lengths of the insulated annular section (a) 20 mm and (b) 80 mm.

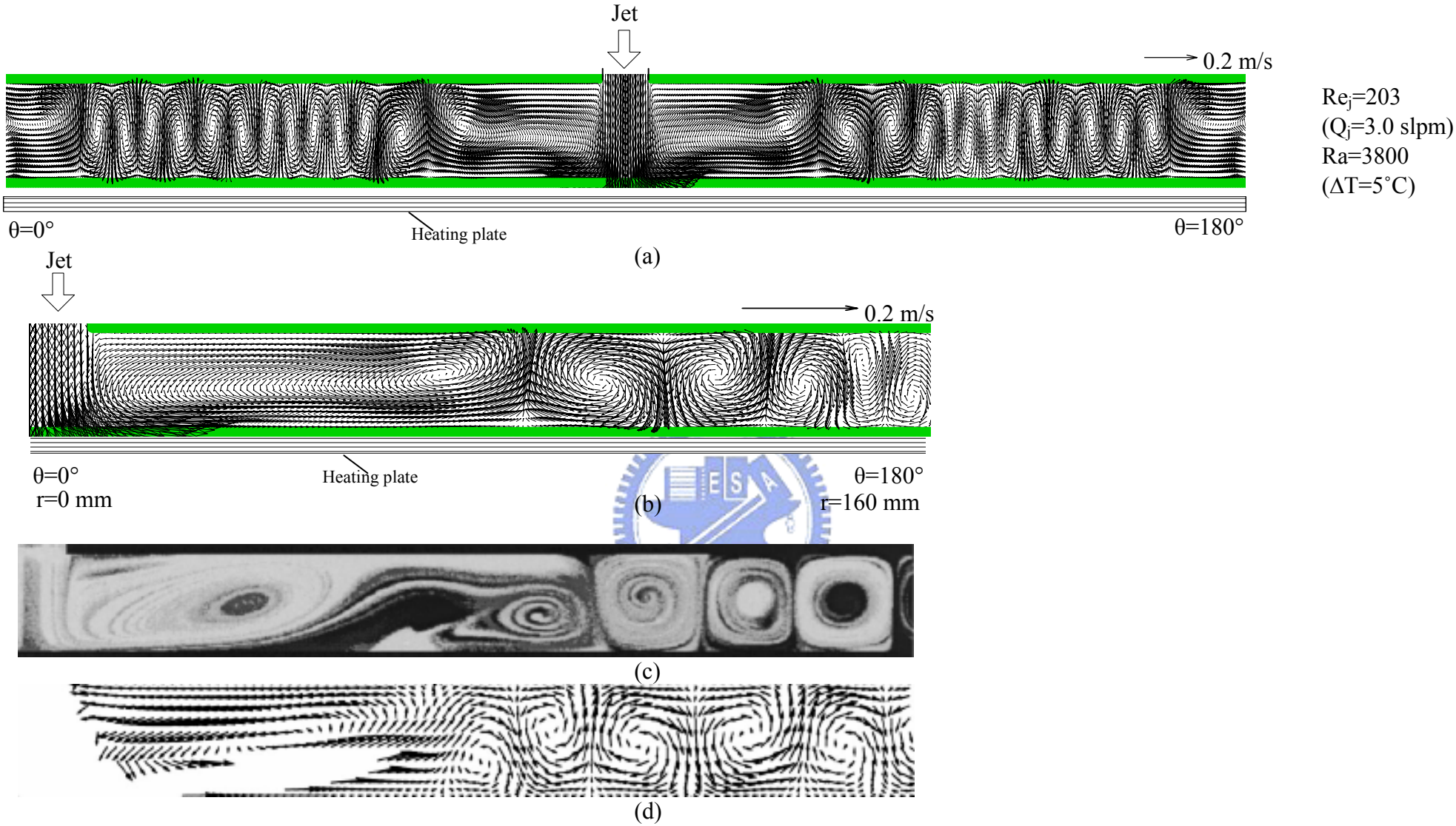

Fig. 3.12 Transient vortex flow for the case with D = 500 m, D_j = 20.0 mm, H = 20.0 mm, Re_j = 203 (Q_j = 3 slpm) and Ra = 3800 (ΔT=5˚C): (a) our predicted velocity vectors on the cross plane $\theta = 0^{\circ}$ & 180° at t = 9 sec., and (b) our predicted velocity vectors on the plane $\theta = 180^{\circ}$ at t = 9 sec., (c) side view flow photo at $\theta = 180^{\circ}$ from Santen et al. (2000), and (d) numerically computed vortex flow at $\theta = 180^{\circ}$ from Santen et al. (2000).